Journal of Materials Chemistry A

Reaction mechanism and kinetics for N2 reduction to ammonia on the Fe-Ru dual atom catalysts

Journal:	*Journal of Materials Chemistry A*
Manuscript ID	TA-ART-08-2022-006826.R1
Article Type:	Paper
Date Submitted by the Author:	02-Oct-2022
Complete List of Authors:	Rehman, Faisal; Hong Kong University of Science and Technology School of Engineering, Chemical and biological engineering Kwon, Soonho; California Institute of Technology Hossain, Md Delowar; Hong Kong University of Science and Technology, Department of Chemical and Biological Engineering, Musgrave , Charles; California Institute of Technology, Center for Materials and Molecular Simulation Goddard, William; CALTECH, Beckman Institute, Center for Materials and Molecular Simulation Luo, Zhengtang; Hong Kong University of Science and Technology, Department of Chemical and Biomolecular Engineering,

Reaction mechanism and kinetics for N_2 reduction to ammonia on the Fe-Ru dual atom catalysts

Faisal Rehman [a,b,c], Soonho Kwon [c], Md Delowar Hossain [d], Charles B. Musgrave III [c]
William A. Goddard III [c*], Zhengtang L.U.O. [a*]

[a] *Department of Chemical and Biological Engineering, Guangdong-Hong Kong-Macao Joint Laboratory for Intelligent Micro-Nano Optoelectronic Technology, William Mong Institute of Nano Science and Technology, and Hong Kong Branch of Chinese National Engineering Research Center for Tissue Restoration and Reconstruction, the Hong Kong University of Science and Technology, Clear Water Bay, Kowloon, Hong Kong, 999077, P.R. China*

[b] *Department of Chemical & Polymer Engineering, University of Engineering & Technology Lahore, Faisalabad Campus, 3.5 km, Khurrianwala - Makkuana By-Pass, Faisalabad, Pakistan.*

[c] *Materials and Process Simulation Center (M.S.C.), MC 139-74, California Institute of Technology, Pasadena CA, 91125, U.S.A.*

[d] *SUNCAT Center for Interface Science and Catalysis, Department of Chemical Engineering, Stanford University, Stanford, CA 94305, U.S.A.*

[*] *Email:* wag@caltech.edu (**W.A.G**) and keztluo@ust.hk (**Z.L.**)

ORCID-WAG-0000-0003-0097-5716

Abstract: 248 words

Environmental and energy considerations demand that Haber-Bosch process for reducing N_2 to NH_3 by replaced with electrochemical ammonia synthesis where the H atoms come from water instead of from H_2. But a practical realization of electrochemical N_2 reduction reaction (NRR) requires the development of new generation electrocatalysts with low overpotential and high Faraday efficiency (FE). A major problem here is that the hydrogen evolution reaction (HER) competes with NRR. Herein, we consider new generation dual-site catalysts involving two different metals incorporated into a novel two-dimensional C_3N-C_2N heterostructure that provides a high concentration of well-defined but isolated active sites that bind two distinct metal atoms to enable specific electrochemical reactions while in a framework that facilitates electron transfer. We report here the mechanism and predicted kinetics as a function of applied potential for both NRR and HER for the (Fe-Ru)/ C_3N-C_2N dual atom catalyst. These calculations employ the grand canonical potential kinetics (GCP-K) methodology to predict reaction free energies and reaction barriers as a function of applied potential. The rates are then used in a microkinetic model to predict the turn-over-frequencies (TOF) as a function of applied potential. At U= 0 V, the FE for NRR is 93%, but the current is only 2.0 mA/cm^2. The onset potential (at 10 mA/cm^2) for ammonia on Fe-Ru/C_3N-C_2N is -0.22 V_{RHE}. This leads to a calculated TOF of 434 h^{-1} per Fe-Ru site. We expect that the mechanisms for NRR and HER developed here will help lead to new generations of NRR with high TOF and FE.

Key words: N_2 reduction, reaction kinetics, electrochemical ammonia synthesis, dual-atom catalyst.

1. Introduction

Converting abundantly available nitrogen (N_2) to ammonia (NH_3) is a most important industrial reaction. NH_3 is a key ingredient in developing nitrate fertilizers, making NRR imperative for combating global increasing food demands [1], [2], [3]. NH_3 also has potential as a carbon-free fuel alternative, and as an H_2 storage material [4]. Since 1915, the energy-intensive Haber-Bosch (HB) process has been the dominant route for the industrial-scale synthesis of NH_3. However, HB is extremely energy intensive, accounting for ~2% of global energy consumption. Additionally, the water gas shift process to produce the H_2 required produces over 1% of the world's CO_2 emissions [5] [6]. To address these environmental issues, while sustaining human society, it is essential to develop a green process for NRR.

The electrochemical N_2 reduction reaction (NRR) to NH_3 allows the H required to be obtained from H_2O, an alternative that can provide zero carbon footprint for NH_3 synthesis. This green process is more energy-efficient than the HB process by about 20% [7]. Numerous electrocatalysts have shown NRR activity under ambient conditions, but the low FE (~10%) and activity are far too low for industrial realization [8]. The sluggish rate of the electrochemical NRR arises from the stability of N_2, while poor selectivity is due to the competing hydrogen evolution reaction (HER), which is prominent at the negative potentials optimal for NRR. Specifically, increased HER has been attributed to the dominance of H coverage at more negative potential [8], [9]. This leads to a decrease in the NRR current and an increase in the HER current under ambient conditions. To understand the interplay of HER and NRR activity, a fundamental understanding of potential-dependent reaction kinetics and coverage is required [7].

Herein, we design a novel two-dimensional C_3N-C_2N heterostructure (Figure 1) that provides a well-defined active site to bind a pair of metal atoms next to each other to enable more selective electrochemical reactions. The C_3N-C_2N provides a high concentration of isolated sites while facilitating electron transfer efficiently [11], [12]. Each isolated site provides a hexagonal cavity with six sp^2 N atoms that can bind two metal atoms. In previous reports, Fe and Ru-based single atom catalysts supported on various 2D substrates exhibited relatively high NH_3 yield and FE [13]–[16]. With this in mind, we examine the C_3N-C_2N embedded with 1 Fe and 1 Ru atom as a novel dual-atom catalyst (DAC) for electrochemical conversion of N_2 to NH_3.

We report here the predicted kinetics under acidic conditions of NRR and HER using C_3N-C_2N nanosheet containing Fe and Ru- (Fe-Ru/C_3N-C_2N). We find that the onset potential (for a current density of 10 mA/cm^2) for producing NH_3 on the Fe-Ru/C_3NC_2N surface is -0.22 V *vs* RHE with a turnover frequency (TOF) of 434 h^{-1} per Fe-Ru site. This can be compared to the onset potential of -0.14 V for HER at the same site, leading to a FE of 10.53% towards NH_3.

2. Grand Canonical Quantum Mechanics Formulation:

We need a comprehensive understanding of how NRR and HER depend on applied potential to develop more efficient and selective catalysts. To probe the intermediate steps and barriers of the reaction mechanism, we utilize quantum mechanics (QM). However, typical QM is limited to a fixed charge, whereas electrochemical reactions occur at a fixed potential. That is, the initial state, transition state, and product state for each reaction step should be at the same applied potential. To keep the potential constant, the charge near the active site will change as the reaction proceeds from the initial state through the transition state to the product. Keeping the chemical potential constant as the QM wavefunction and structure is optimized along the reaction path is complex and time-consuming. Recently, we developed the Grand Canonical Potential Kinetics (GCP-K) methodology to simplify this process into a very efficient procedure. In GCP-K, the free energy, *F(n)*, is calculated for each reaction step using standard QM as a function of the net charge. We then apply a Legendre transformation (Equation 1) to convert from *F(n)* to the grand canonical free energy, *G(n: U)*:

$$G(n; U) = F(n) - ne\,(U_{SHE} - U) \qquad \textit{(Equation 1)}$$

For each potential (U), the number of electrons is optimized to minimize *G(n; U)*, leading finally to the grand canonical potential, *GCP(U)*, where the number of electrons depends implicitly on U [17], [18], [19].

The accuracy of GCP-K was recently validated for the oxygen evolution reaction on single crystal Co/TiO_2 nanoparticles with isolated Co sites [20], where the predicted TOF versus U agreed remarkably well with the experimentally predicted rate. Thus, GCPK leads to TOF = 13.1 s^{-1} at η=300 mV per Co and TOF = 307.4 s^{-1} at η=400 mV and Tafel slope of 74 mV/dec, Compared to experiment: TOF = 9.1 s^{-1} at η=300 mV per Co; TOF = 249.2 s^{-1}, at η=400 mV; and Tafel slope of 72 mV/dec. Assuming all surface Co are active, this indicates that the overall free energy activation barrier from GCPK is low by ~0.03 eV.

GCP-K has also been applied to HER on single-layer WSe_2 and WTe_2 chalcogenides, where single Se/Te vacancies lead to four intermediates (0−3 H at the vacancy). The predicted onset potential (at 10 mA/cm^2) is −0.53 V_{RHE} for WSe_2 (experimental value is −0.51 V_{RHE} [21]), and −0.51 V_{RHE} for WTe_2 (experimental value is −0.57 V_{RHE} [22]), validating the accuracy of GCP-K [23].

2.1 Methodology:

Structure optimizations were carried out at several fixed charges for each step using the PBE-D3 flavor of Density Functional Theory (DFT) with VASPsol implicit solvation [24]–[29]. The cutoff energy for the plane wave basis set was 450 eV. The structure optimization criteria were 1×10^{-6} eV for the energy and 0.02 eV/Å for the forces on each atom, while 0.04 eV/Å was used for the transition state (CI-NEB) calculations. The K-point grid used for geometry optimizations and energy calculations was 2 × 5 × 1. The vibrational modes were calculated at 298.15 K to obtain the zero-point energy, entropy, and Temperature corrections to enthalpy.

To better describe the proton transfer from solvated hydronium ion (H_3O^+) to the reactant, we included two explicit water molecules to stabilize the hydronium ion, along with the implicit solvation model as implemented in VASPsol. We applied the CI-NEB method from the VTST package to determine transition states [30], [31]. For the reaction barriers, we performed free energy calculations for each point along the NEB path to allow the structure of the transition state to change as a function of applied potential.

After obtaining the optimized structures, we performed single-point JDFTx calculations using the CANDLE implicit solvation model to obtain the free energy [32], [33]. We then applied the Legendre transformation (1) to get *G(n: U)* and *GCP(U)*.

3. Mechanism for NRR on the (Fe, Ru)/C_3N-C_2N DAC:

Electrochemical NRR requires six proton and electron transfers, which can be achieved through either associative or enzymatic pathways, as shown in Figure S1. We begin by calculating the mechanism for converting N_2 to NH_3 on (Fe,Ru)/C_3N-C_2N at U = 0 V.

3.1 N_2 bonding to surface: end on and side on

The first step of the NRR process is for N_2 molecule to bind to the Fe-Ru surface, which can be via end-on or side-on orientations of the N_2 molecule. The calculated adsorption free energy is -21.6 kcal/mol for the end-on configuration and -8.75 kcal/mol for the side-on configuration, indicating that the end-on configuration is far more favorable on the Fe-Ru active site. The effect of applied potential is negligible on the N_2 adsorption because it is not an electrochemical step. When the N_2 binds via the end-on configuration, the N-N bond elongates from its nominal value of 1.10 Å to 1.17 Å, while for the side-on configuration, the N_2 molecule elongates to 1.21 Å.

3.2 Following the associative pathway

3.2a Formation of $*N_2H$

The free energy profile at multiple applied potentials, and the corresponding optimized structures of the associative pathway for the NRR are shown in Figures S2 and S3, respectively. To form $*N_2H$ when the N_2 is chemisorbed to the Fe-Ru dual-site, we introduce an $H_7O_3^+$ cluster (H_3O^+ + 2 H_2O) to the system. In acidic conditions, the proton in the $H_7O_3^+$ cluster reacts with the $*N_2$ molecule to form the $*N_2H$ intermediate while producing a cluster of 3 solvated H_2Os. The reaction free energy to produce $*N_2H$ is $\Delta G = -15.0$ kcal/mol at $U = 0$ V.

3.2b Formation of $*N\text{-}NH_2$ and *HN-NH

After the first protonation, there are two possible pathways for the second protonation:

1. distal pathway to form $*N\text{-}NH_2$, leading to a free energy change of $\Delta G = -16.8$ kcal/mol
2. alternating pathway to form *HN-NH, leading to a free energy change of $\Delta G = -8.81$ kcal/mol at the neutral charge

This indicates that the distal pathway is more favorable on the Fe-Ru site. The optimized structures for these intermediates are depicted in Figure S4.

3.2c Following the distal pathway:

In the distal second protonation step, the adsorbed $*N_2H$ reacts with a proton to form $*N\text{-}NH_2$ intermediate. This step is exergonic step with $\Delta G = -24.8$ kcal/mol (at $U = 0$).

Following $*N\text{-}NH_2$ formation, the proton from $H_7O_3^+$ attacks $*N\text{-}NH_2$ to form $*N\text{-}NH_3$ and 3 H_2O. The free energy of forming $*N\text{-}NH_3$ is -21.3 kcal/mol. The N-N bond length increases with successive protonation steps as the bond goes from being an activated triple bond (1.17 Å) to a double bond (1.34 Å) and to a single bond (1.45 Å).

Next, with $\Delta G = -13.0$ kcal/mol is to break the $N\text{-}NH_3$ bond to release the first NH_3 product molecule, leaving *N on the surface, The resulting *N bridges the Fe and Ru atoms.

The next step is reaction of a proton with *N to form *NH, which is exergonic with a free energy of $\Delta G = -23.3$ kcal/mol.

Next, *NH is protonated to form $*NH_2$ with $\Delta G = -43.1$ kcal/mol.

In the final protonation step, $*NH_2$ reacts with a proton to form $*NH_3$ with $\Delta G = -38.2$ kcal/mol.

Desorbing this second NH_3 from the surface requires an energy of 18.0 kcal/mol.

3.3 Enzymatic pathway:

In the enzymatic pathway for NRR, the N_2 binds to the active site via the side-on configuration [34]. The free energy profile and corresponding optimized structures are shown in Figures S5 and S6.

First the proton from $H_7O_3^+$ attacks the $*N_2$ to form *N-NH and the $(H_2O)_3$ cluster, with $\Delta G = -8.38$ kcal/mol ($U = 0$ V).

Next the *N-NH converts exergonically into *HN-NH by combining with a proton from $H_7O_3^+$, with $\Delta G = -17.97$ kcal/mol.

In the third protonation step, *HN-NH is converted into $*HN\text{-}NH_2$ with $\Delta G = -21.26$ kcal/mol.

The next protonation forms $*NH_2\text{-}NH_2$ with $\Delta G = -67.1$ kcal/mol.

Finally, the first NH_3 molecule forms as $*NH_2\text{-}NH_2$ is protonated, leaving $*NH_2$ on the Fe-Ru surface. This has a $\Delta G = -43.1$ kcal/mol.

The final step is to protonate $*NH_2$, resulting in adsorbed $*NH_3$ at $\Delta G = -38.2$ kcal/mol relative to the starting state.

3.4 Transition states and activation Free energy

3.4a NRR

Figure 2 shows the initial, transition, and final states for conversion of the N_2 to ammonium ion, including how the initial and transition state geometries change with the applied potential. Here we discuss the main reaction steps dominating the reaction kinetics.

Figure 2a shows the initial, transition, and final states for converting $*N\text{-}NH_2$ to $*N\text{-}NH_3$. The transition state of step cd uses H from H_3O^+ to form a new NH bond, leading to an energy barrier of $\Delta G^\dagger = 4.3$ kcal/mol at $U = 0$ V. This reduces to $\Delta G^\dagger = 3.2$ kcal/mole as U changes to -0.2 V. Fig 2b shows the change in the N-H distance of the TS of step cd as a function of applied potential. As U changes from -0.06 to -0.67 V, the N-H bond distance varies from 1.30 Å to 1.58 Å.

The next step (step de) is the cleavage of the $N\text{-}NH_3$ bond, releasing the first ammonia molecule and N left on the surface, a nonelectrochemical step as shown in Fig 2c. The transition state for breaking the $N\text{-}NH_3$ bond requires a relatively high energy barrier of $\Delta G^\dagger = 7.6$ kcal/mol at $U = 0$ V, which reduces to $\Delta G^\dagger = 6.6$ kcal/mol at $U = -0.2$ V.

Figure 2e illustrates the sixth proton-electron transfer step that leads the $*NH_2$ to $*NH_3$. The transition state involves breaking the O-H bond in H_3O^+ while forming a new NH bond of $*NH_2$ leading to an energy barrier of $\Delta G^\dagger = 8.2$ kcal/mol at $U = 0$ V, which drops to 6.6 kcal/mol at $U = -0.2$ V. The N-H bond distance varies from 1.36 Å to 1.40 Å as U changes to -0.02 V to -0.68 V as shown in Figure 2f.

In acidic conditions, the NH_3 molecule in solution converts to the ammonium ion, NH_4^+. Thus, we analyze the barrier required to convert $*NH_3$ molecule to NH_4^+. Figure 2g shows the initial, transition, and final states for step ha, where the proton from $H_7O_3^+$ reacts with the $*NH_3$ to form NH_4^+ and $(H_2O)_3$. The energy barrier arises primarily from breaking the NH_3 bond to the active site while simultaneously inverting the NH_3 molecule to react with the proton. The transition state has an energy barrier of $\Delta G^\dagger = 16.3$ kcal/mol at $U = 0$ V, which reduces to 15.8 kcal/mol at $U = -0.2$ V. Figure 2h shows the changes of bond distance between N of NH_3 and H from bottom H_2O

molecule. As *U* changes from -0.04 to -0.52 V, the N-H bond distance varies from 1.63 Å to 1.78 Å.

3.4b HER:

The hydrogen evolution reaction (HER) is the main competing reaction with NRR, decreasing the FE for NH_3 synthesis. Thus, we must examine the comparative activity of HER and NRR under the same electrochemical conditions. Since our electrocatalytic environment is acidic (pH = 1), the favorable pathway for HER on the Fe-Ru dual site is the sequential binding of three protons by Volmer reactions, each followed by H_2 evolution via the Tafel mechanism.

First, the proton from the $H_7O_3^+$ cluster moves toward the active site and adsorbs on the Fe-Ru surface via the Volmer reaction, as shown in Figure 3a. This is an exergonic step with a free energy of $\Delta G = -11.9$ kcal/mol at $U = 0$ V. This Volmer reaction (step ai) shows a minimum energy barrier of $\Delta G^{\dagger} = 1.7$ kcal/mol at $U = 0$ V, which reduces to $\Delta G^{\dagger} = 0.7$ kcal/mol at $U = -0.2$ V. The transition state has +0.23 more charge than the initial state, while the final state has 0.42 more charge than the transition state, for a total of 0.65 charge transfer at $U = 0$ V, changes to 0.62 at $U = -0.2$ V.

The second step involves the adsorption of the second proton on the Fe-Ru site with a free energy value of $\Delta G = -17.6$ kcal/mol at $U = 0$ V. The initial, transition, and final states of step ij are shown in Fig 3c. The barrier at the TS reduces from $\Delta G^{\dagger} = 1.2$ to 0.7 kcal/mol as *U* shifts from 0 to -0.2 V. The TS has 0.46 more charge than the IS, while the final state has 0.38 more charge than the TS, with a net charge transfer of 0.84 at $U = 0$.

The third step is the adsorption of the third proton on the Fe-Ru surface from the solvent via the Volmer step as shown in Fig 3e. The energy barrier for the TS is $\Delta G^{\dagger} = 5.5$ kcal/mol at $U = 0$ V which decreases to $\Delta G^{\dagger} = 4.9$ kcal/mol at $U = -0.2$ V.

The Tafel reaction is a nonelectrochemical step where the two adsorbed protons evolve from Fe-Ru surface to produce H_2 leaving one proton on the surface. The energy barrier required for the Tafel step is $\Delta G^{\dagger} = 9.7$ kcal/mol at $U = 0$ V. Normally, the GCP barrier for the Tafel step increases slowly as the applied potential becomes more negative. Indeed, $\Delta G^{\ddagger} = 10.7$ kcal/mol at $U = -0.2$ V.

All GCP barriers of NRR and HER for the Fe-Ru surface as a function of applied potential are illustrated in Figure 4.

3.5 Effect of applied potential on N_2 and H coverage;

To analyze how applied potential affects N_2 and H binding to the Fe-Ru site, Figure 5 compares the free energy change of $*N_2$ and *H adsorption as a function of applied potential, the first reaction steps for NRR and HER, respectively. At $U = 0$ V, N_2 adsorption has $\Delta G = -20.1$ kcal/mol, while H adsorption is $\Delta G = -11.9$ kcal/mol, indicating that N_2 adsorption is more favorable close to the equilibrium potential of NRR at standard conditions (0.057 V vs RHE). As the applied potential becomes more negative, both adsorptions become more favorable. However, because N_2 adsorption is not an electrochemical step, the change in adsorption free energy for $*N_2$ is small compared to that of *H at more negative potential. The ΔG vs *U* slope for $*N_2$ is 1.9, while for *H the slope is 20.3, indicating H adsorption is far more sensitive to *U*. Due to the difference in slopes, a crossover occurs at $U_{cross} = -0.53$ V, where the N_2 and H adsorption free energies become equal. This analysis indicates the strong dependency of H and N_2 coverage on the applied potential, where H coverage begins to dominate N_2 coverage at $U < U_{cross}$.

4. NRR and HER Kinetics:

We evaluated the N_2 reduction reaction and hydrogen evolution reaction at acidic condition (pH = 0) on Fe-Ru/C_3N-C_2N DAC. We summarize the reaction free energies and free energy activation barriers as a function of applied potential obtained by GCP-K for NRR and HER in Figure 6. We developed a microkinetic model to examine how NRR and HER activity depend on the applied potential. With the GCP calculated for all intermediates and transition states, we use the Eyring equation (Equation 2) to predict potential-dependent rate constants, $k_{ij}(U)$:

$$k_{ij}(U) = \frac{k_B T}{h} \exp\left(\frac{-\Delta G_{ij}^{\ddagger}(U)}{k_B T}\right) \qquad \text{(Equation 2)}$$

We built the microkinetic model using these rate constants to predict the concentrations of the various species and overall reaction kinetics as a function of applied potential. The rate laws for each species are written as in (3):

$$\frac{dx_a}{dt} = k_{ba}x_b + k_{ha}x_h + k_{ia}x_i - (k_{ab} + k_{ai})x_a \qquad (3)$$

$$\frac{dx_b}{dt} = k_{ab}x_a + k_{cb}x_c - (k_{ba} + k_{bc})x_b$$

$$\frac{dx_c}{dt} = k_{bc}x_b + k_{dc}x_d - (k_{cb} + k_{cd})x_c$$

$$\frac{dx_d}{dt} = k_{cd}x_c - (k_{dc} + k_{de})x_d$$

$$\frac{dx_e}{dt} = k_{de}x_d + k_{fe}x_f - k_{ef}x_e$$

$$\frac{dx_f}{dt} = k_{ef}x_e + k_{gf}x_g - (k_{fe} + k_{fg})x_f$$

$$\frac{dx_g}{dt} = k_{fg}x_f + k_{hg}x_h - (k_{gf} + k_{gh})x_g$$

$$\frac{dx_h}{dt} = k_{gh}x_g - (k_{hg} + k_{ha})x_h$$

$$\frac{dx_i}{dt} = k_{ai}x_a + k_{ji}x_j + k_{ki}x_k - (k_{ia} + k_{ij})x_i$$

$$\frac{dx_j}{dt} = k_{ij}x_i + k_{kj}x_k - (k_{ji} + k_{jk})x_j$$

$$\frac{dx_k}{dt} = k_{jk}x_j - (k_{kj} + k_{ki})x_k$$

Here x represents the concentration of each species as in Figure 5, $k_{ij}(U)$ is the rate constant as a function of applied potential (calculated from equation (2)), k_B is the Boltzmann constant, h is

Plank's constant, and $\Delta G_{ij}^{\ddagger}(U)$ is the potential dependent free energy barrier for reaction ij. For the steady-state kinetics, the left-hand sides of all rate laws are set to 0, and we apply the constraint, $\Sigma_i x_i = 1$ (mole fractions sum to 1). Solving the linear equations simultaneously, we obtain the species concentrations as shown in Table 1 and the rates as a function of applied potential. The species concentrations vary with the applied potential. The NH_3 and H_2 partial current densities are shown in Figure 7.

Figure 7a shows the NH_4^+ current density (I) as a function of applied potential for the Fe-Ru DAC. This shows that the NRR for the Fe-Ru site has an onset potential (10 mA cm^{-2}) of -0.22 V. At *U* = -0.22 V, we calculate a TOF of 434 h^{-1} with FE = 10.53 % for NRR.

The I-V curve for HER is depicted in Figure 7b, showing that 10 mA/cm^2 can be achieved at -0.14 V. The current density for NH_3 and HER both increase for more negative applied potential, but the rate of increasing HER current is much faster than that of NH_3 current, reducing the FE towards NH_3 at more negative potential (Figure 7c). This trend is generally expected since the *H coverage increases and the HER barrier decreases at more negative potential, reducing the N_2RR activity.

The rate-determining step for the NRR process is desorption of the second NH_3 molecule and its conversion to NH_4^+ which requires a barrier of 16.3 kcal/mol. To further improve the entire electrochemical system for NH_3 synthesis, it is essential to find active sites, promoters, and electrolytes that improve the NRR selectivity over HER.

5. Conclusions:

In summary, we investigated the reaction mechanism and kinetics for NRR and HER on the dual atom (Fe,Ru)/C_3N-C_2N catalyst using grand canonical potential kinetics. GCP-K considers the reactant, reaction pathway and product to all be at the same applied potential for all reactions, mimicking the experimental situation. Thus, the electrons rearrange locally in response to the reaction events.

We find that NRR preferably follows the associative pathway for NH_3 synthesis at the Fe-Ru site with NH_3 desorption the rate-determining step, requiring a barrier of $\Delta G^{\dagger} = 16.3$ kcal/mol. Overall, NRR is -16.6 kcal/mol downhill. The FE at *U*=0 is 93% but the current is only 2 mA/cm^2. We predict that an NH_3 onset current density of 10 mA/cm^2 can be achieved at the Fe-Ru site at a low overpotential of -0.22 V v*s* RHE, with a turnover frequency (TOF) for NH_3 production of 434 h^{-1} per Fe-Ru site. But the FE drops to 10.53% for NH_3 production.

In addition to NRR, the Fe-Ru surface also leads to high activity for HER, with an onset current density of 10 mA/cm^2 at -0.14 V.

The microkinetic model shows how NRR and HER depend on the applied potential, explaining the decline in NRR activity for more negative potentials due to increased selectivity towards HER. We expect that the mechanisms for NRR and HER developed here will help lead to new generations of NRR with high TOF and FE.

Acknowledgements:

Z.L. acknowledge supports by the RGC (16304421), the Innovation and Technology Commission (ITC-CNERC14SC01), Guangdong Science and Technology Department (Project#:2020A0505090003), Research Fund of Guangdong-Hong Kong-Macao Joint Laboratory for Intelligent Micro-Nano Optoelectronic Technology (No. 2020B1212030010), IER foundation

(HT-JD-CXY-201907), and Shenzhen Special Fund for Central Guiding the Local Science and Technology Development (2021Szvup136). F. R. appreciates financial support from the Higher Education Commission (HEC) of Pakistan. The Caltech activities were supported by the Liquid Sunlight Alliance, which is supported by the U.S. Department of Energy, Office of Science, Office of Basic Energy Sciences, Fuels from Sunlight Hub under Award Number DE-SC0021266. All results and findings in this work reflect solely the opinions of the author and does not represent the views of the U.S. government.

References:

[1] J. Rockström *et al.*, "A safe operating space for humanity," *Nat. 2009 4617263*, vol. 461, no. 7263, pp. 472–475, Sep. 2009, doi: 10.1038/461472a.

[2] V. Smil, "Enriching the Earth: Fritz Haber, Carl Bosch, and the Transformation of World Food Production," *Enrich. Earth*, Dec. 2000, doi: 10.7551/MITPRESS/2767.001.0001.

[3] J. W. Erisman, M. A. Sutton, J. Galloway, Z. Klimont, and W. Winiwarter, "How a century of ammonia synthesis changed the world," *Nat. Geosci. 2008 110*, vol. 1, no. 10, pp. 636–639, Sep. 2008, doi: 10.1038/ngeo325.

[4] V. Smil, "Detonator of the population explosion," *Nat. 1999 4006743*, vol. 400, no. 6743, pp. 415–415, Jul. 1999, doi: 10.1038/22672.

[5] C. J. M. Van Der Ham, M. T. M. Koper, and D. G. H. Hetterscheid, "Challenges in reduction of dinitrogen by proton and electron transfer," *Chem. Soc. Rev.*, vol. 43, no. 15, pp. 5183–5191, Jul. 2014, doi: 10.1039/C4CS00085D.

[6] "Insights Series 2017 - Renewable Energy for Industry – Analysis - IEA." https://www.iea.org/reports/renewable-energy-for-industry (accessed Jun. 20, 2022).

[7] "Ammonia as an Alternative Energy Storage Medium for Hydrogen Fuel Cells: Scientific and Technical Review for Near-Term Stationary Power Demonstration Projects, Final Report." https://escholarship.org/uc/item/7z69v4wp (accessed May 02, 2022).

[8] F. Rehman, M. Delowar Hossain, A. Tyagi, D. Lu, B. Yuan, and Z. Luo, "Engineering electrocatalyst for low-temperature N2 reduction to ammonia," *Mater. Today*, vol. 44, pp. 136–167, Apr. 2021, doi: 10.1016/J.MATTOD.2020.09.006.

[9] A. R. Singh *et al.*, "Electrochemical Ammonia Synthesis - The Selectivity Challenge," *ACS Catal.*, vol. 7, no. 1, pp. 706–709, Jan. 2017, doi: 10.1021/ACSCATAL.6B03035/ASSET/IMAGES/LARGE/CS-2016-03035F_0001.JPEG.

[10] L. Hu, Z. Xing, and X. Feng, "Understanding the Electrocatalytic Interface for Ambient Ammonia Synthesis," *ACS Energy Lett.*, vol. 2020, pp. 430–436, 2020, doi: 10.1021/ACSENERGYLETT.9B02679/ASSET/IMAGES/LARGE/NZ9B02679_0004.JPEG.

[11] S. Chen *et al.*, "Design of a Graphene Nitrene Two-Dimensional Catalyst Heterostructure Providing a Well-Defined Site Accommodating One to Three Metals, with Application to CO2 Reduction Electrocatalysis for the Two-Metal Case," *J. Phys. Chem. Lett.*, vol. 11, no. 7, pp. 2541–2549, Apr. 2020, doi:

10.1021/ACS.JPCLETT.0C00642/SUPPL_FILE/JZ0C00642_LIVESLIDES.MP4.

[12] W. Xu, C. Chen, C. Tang, Y. Li, and L. Xu, "Design of Boron Doped C2N-C3N Coplanar Conjugated Heterostructure for Efficient HER Electrocatalysis," *Sci. Reports 2018 81*, vol. 8, no. 1, pp. 1–9, Apr. 2018, doi: 10.1038/s41598-018-24044-4.

[13] "2018 - Advanced Materials - Achieving a Record-High Yield Rate of 120.9 μgNH3mgcat.−1h−1 for N2 Electrochemical Reduction over Ru S.pdf."

[14] M. Wang *et al.*, "Over 56.55% Faradaic efficiency of ambient ammonia synthesis enabled by positively shifting the reaction potential," *Nat. Commun. 2019 101*, vol. 10, no. 1, pp. 1–8, Jan. 2019, doi: 10.1038/s41467-018-08120-x.

[15] Y. Wang *et al.*, "Rational Design of Fe-N/C Hybrid for Enhanced Nitrogen Reduction Electrocatalysis under Ambient Conditions in Aqueous Solution," *ACS Catal.*, vol. 9, no. 1, pp. 336–344, Jan. 2019, doi: 10.1021/ACSCATAL.8B03802/ASSET/IMAGES/LARGE/CS-2018-038023_0005.JPEG.

[16] C. He *et al.*, "Identification of FeN4 as an Efficient Active Site for Electrochemical N2 Reduction," *ACS Catal.*, vol. 9, no. 8, pp. 7311–7317, Aug. 2019, doi: 10.1021/ACSCATAL.9B00959/ASSET/IMAGES/LARGE/CS-2019-00959E_0004.JPEG.

[17] R. Sundararaman, W. A. Goddard, and T. A. Arias, "Grand canonical electronic density-functional theory: Algorithms and applications to electrochemistry," *J. Chem. Phys.*, vol. 146, no. 11, p. 114104, Mar. 2017, doi: 10.1063/1.4978411.

[18] Y. Huang, R. J. Nielsen, and W. A. Goddard, "Reaction Mechanism for the Hydrogen Evolution Reaction on the Basal Plane Sulfur Vacancy Site of MoS 2 Using Grand Canonical Potential Kinetics," *J. Am. Chem. Soc.*, vol. 140, no. 48, pp. 16773–16782, Dec. 2018, doi: 10.1021/JACS.8B10016/ASSET/IMAGES/LARGE/JA-2018-10016M_0008.JPEG.

[19] M. D. Hossain, Y. Huang, T. H. Yu, W. A. Goddard, and Z. Luo, "Reaction mechanism and kinetics for CO2 reduction on nickel single atom catalysts from quantum mechanics," *Nat. Commun. 2020 111*, vol. 11, no. 1, pp. 1–14, May 2020, doi: 10.1038/s41467-020-16119-6.

[20] C. Liu *et al.*, "Oxygen evolution reaction over catalytic single-site Co in a well-defined brookite TiO2 nanorod surface," *Nat. Catal. 2020 41*, vol. 4, no. 1, pp. 36–45, Dec. 2020, doi: 10.1038/s41929-020-00550-5.

[21] M. S. Sokolikova, P. C. Sherrell, P. Palczynski, V. L. Bemmer, and C. Mattevi, "Direct solution-phase synthesis of 1T' WSe2 nanosheets," *Nat. Commun. 2019 101*, vol. 10, no. 1, pp. 1–8, Feb. 2019, doi: 10.1038/s41467-019-08594-3.

[22] H. Kwon *et al.*, "Role of anionic vacancy for active hydrogen evolution in WTe2," *Appl. Surf. Sci.*, vol. 515, p. 145972, Jun. 2020, doi: 10.1016/J.APSUSC.2020.145972.

[23] J. Song, S. Kwon, M. D. Hossain, S. Chen, Z. Li, and W. A. Goddard, "Reaction Mechanism and Strategy for Optimizing the Hydrogen Evolution Reaction on Single-Layer 1T′ WSe2and WTe2Based on Grand Canonical Potential Kinetics," *ACS Appl. Mater. Interfaces*, vol. 13, no. 46, pp. 55611–55620, Nov. 2021, doi:

10.1021/ACSAMI.1C14234/ASSET/IMAGES/LARGE/AM1C14234_0007.JPEG.

[24] K. Mathew, R. Sundararaman, K. Letchworth-Weaver, T. A. Arias, and R. G. Hennig, "Implicit solvation model for density-functional study of nanocrystal surfaces and reaction pathways," *J. Chem. Phys.*, vol. 140, no. 8, p. 084106, Feb. 2014, doi: 10.1063/1.4865107.

[25] S. Grimme, J. Antony, S. Ehrlich, and H. Krieg, "A consistent and accurate ab initio parametrization of density functional dispersion correction (DFT-D) for the 94 elements H-Pu," *J. Chem. Phys.*, vol. 132, no. 15, p. 154104, Apr. 2010, doi: 10.1063/1.3382344.

[26] G. Kresse and J. Furthmüller, "Efficiency of ab-initio total energy calculations for metals and semiconductors using a plane-wave basis set," *Comput. Mater. Sci.*, vol. 6, no. 1, pp. 15–50, Jul. 1996, doi: 10.1016/0927-0256(96)00008-0.

[27] G. Kresse and J. Furthmüller, "Efficient iterative schemes for *ab initio* total-energy calculations using a plane-wave basis set," *Phys. Rev. B*, vol. 54, no. 16, p. 11169, Oct. 1996, doi: 10.1103/PhysRevB.54.11169.

[28] P. E. Blöchl, "Projector augmented-wave method," *Phys. Rev. B*, vol. 50, no. 24, p. 17953, Dec. 1994, doi: 10.1103/PhysRevB.50.17953.

[29] K. Mathew, V. S. C. Kolluru, S. Mula, S. N. Steinmann, and R. G. Hennig, "Implicit self-consistent electrolyte model in plane-wave density-functional theory," *J. Chem. Phys.*, vol. 151, no. 23, p. 234101, Dec. 2019, doi: 10.1063/1.5132354.

[30] D. Sheppard, P. Xiao, W. Chemelewski, D. D. Johnson, and G. Henkelman, "A generalized solid-state nudged elastic band method," *J. Chem. Phys.*, vol. 136, no. 7, p. 074103, Feb. 2012, doi: 10.1063/1.3684549.

[31] G. Henkelman, B. P. Uberuaga, and H. Jónsson, "A climbing image nudged elastic band method for finding saddle points and minimum energy paths," *J. Chem. Phys.*, vol. 113, no. 22, p. 9901, Nov. 2000, doi: 10.1063/1.1329672.

[32] R. Sundararaman, K. Letchworth-Weaver, K. A. Schwarz, D. Gunceler, Y. Ozhabes, and T. A. Arias, "JDFTx: Software for joint density-functional theory," *SoftwareX*, vol. 6, pp. 278–284, Jan. 2017, doi: 10.1016/J.SOFTX.2017.10.006.

[33] R. Sundararaman and W. A. Goddard, "The charge-asymmetric nonlocally determined local-electric (CANDLE) solvation model," *J. Chem. Phys.*, vol. 142, no. 6, p. 064107, Feb. 2015, doi: 10.1063/1.4907731.

[34] Y. Q. Le, J. Gu, and W. Q. Tian, "Nitrogen-fixation catalyst based on graphene: every part counts," *Chem. Commun.*, vol. 50, no. 87, pp. 13319–13322, Oct. 2014, doi: 10.1039/C4CC01950D.

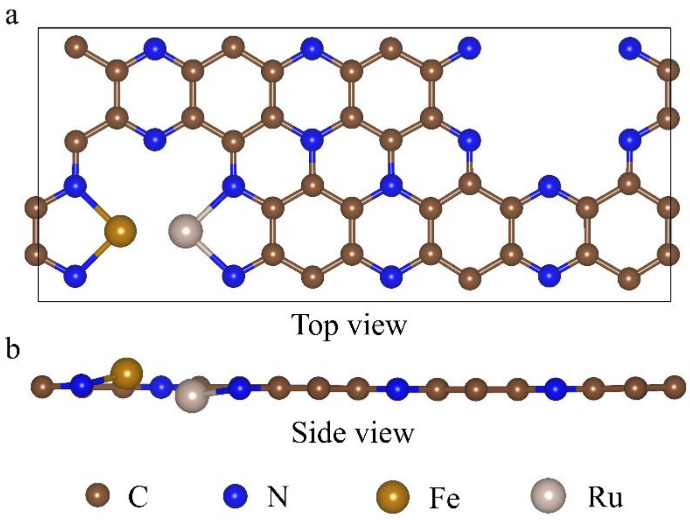

Figure 1: Fe-Ru@C_3N-C_2N optimized structural model**. (a)** Top view of structure model, (**b)** Side of the structural model. Two metal atoms, Fe and Ru are anchored on the moiety side.

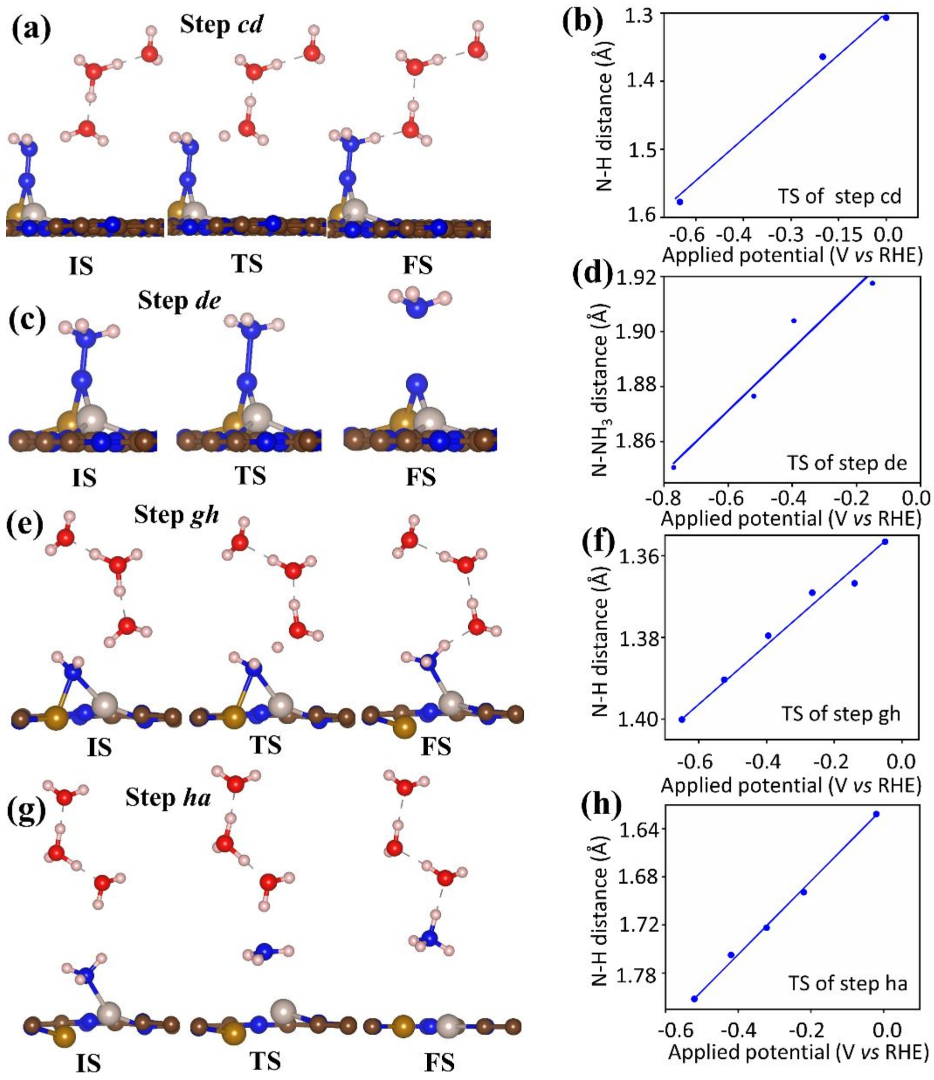

Figure 2: Optimized structures in initial, transition, and final states for NNR Associative pathway and the effect of applied potential on the geometry change on the transition state. The transition state moves towards initial state as more negative potential applied. **(a)** Reaction pathway of step cd, **(b)** N-H bond distance variation of TS of step cd. **(c)** Reaction pathway of step de, **(d)** N-N bond distance variation of TS of step de. **(e)** Reaction pathway of step gh, **(f)** N-H bond distance variation of TS of step gh. **(g)** Reaction pathway of step ha, **(h)** N-H bond distance variation of TS step ha. IS = Initial state, TS = transition state, FS = Final state

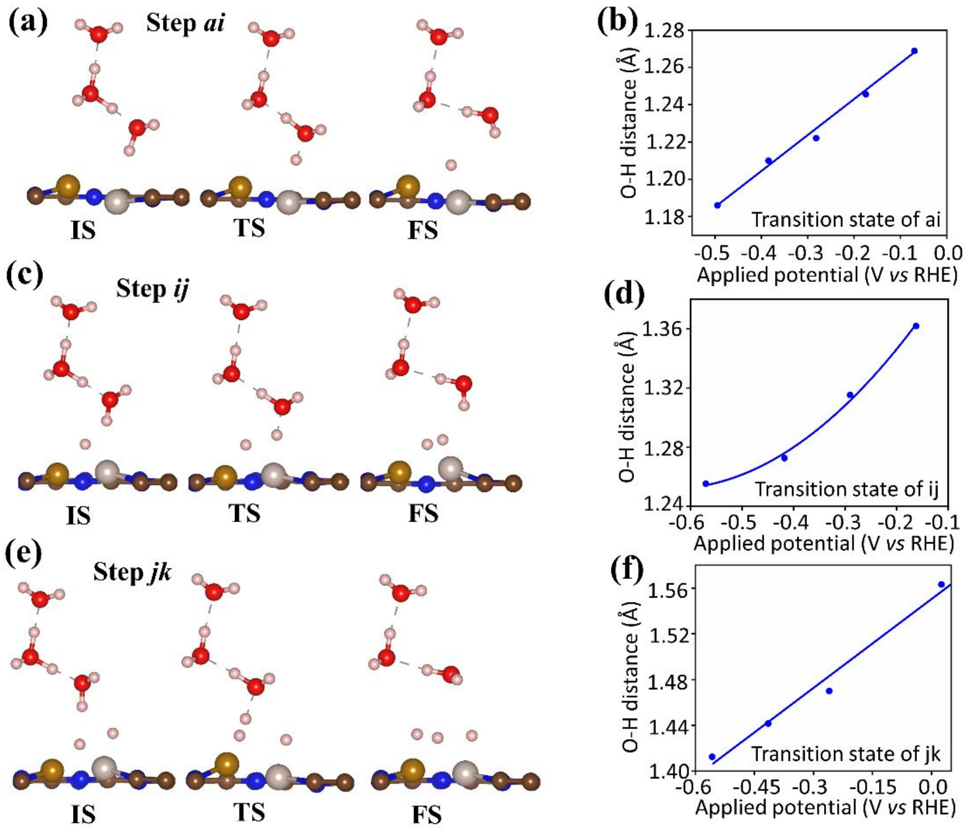

Figure 3: Optimized structures in initial, transition and final states for HER, and the effect of applied potential on the transition state. The transition state moves towards initial state as more negative potential applied. (a) Reaction pathway of step ai, (b) O-H bond distance variation of TS as function of *U* of step ai. (c) Reaction pathway of step ij, (d) O-H bond distance variation of TS as function of *U* of step ij. (e) Reaction pathway of step jk, (f) O-H bond distance variation of TS as function of *U* of step jk.

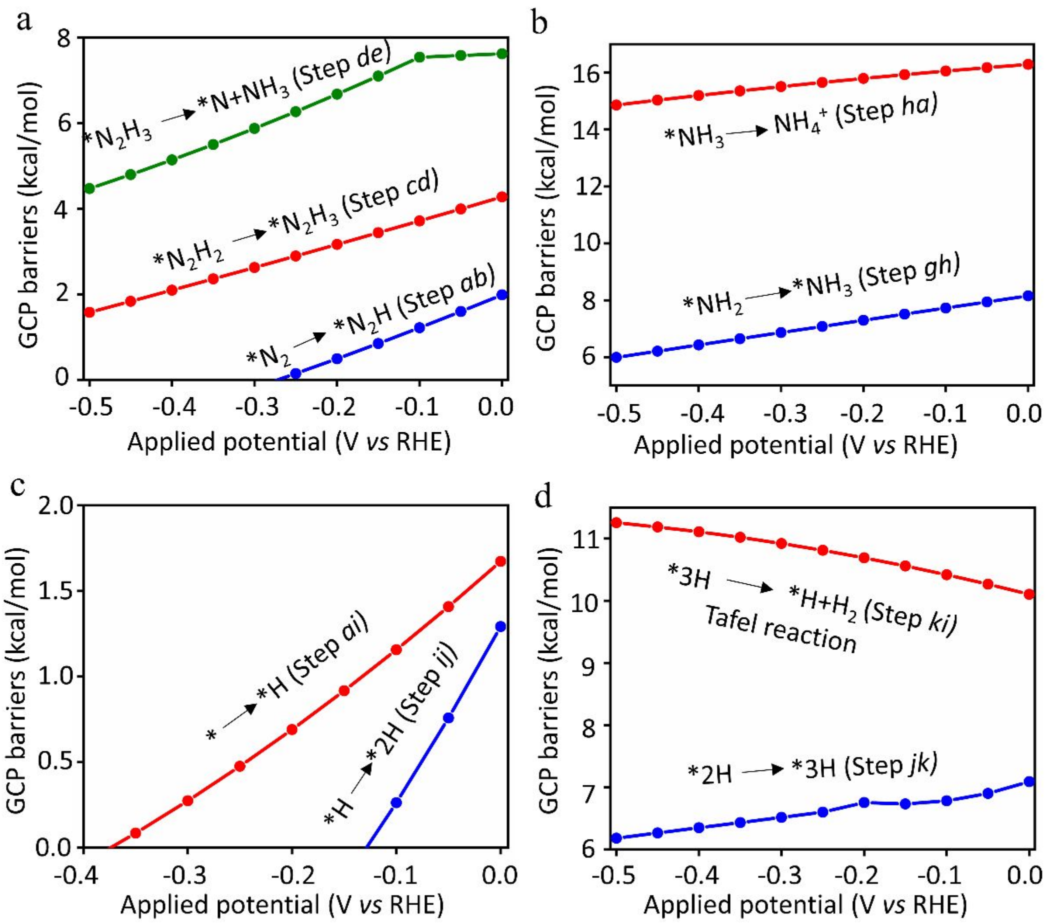

Figure 4: GCP barriers for the NRR and HER electrochemical reactions as a function of applied potential.

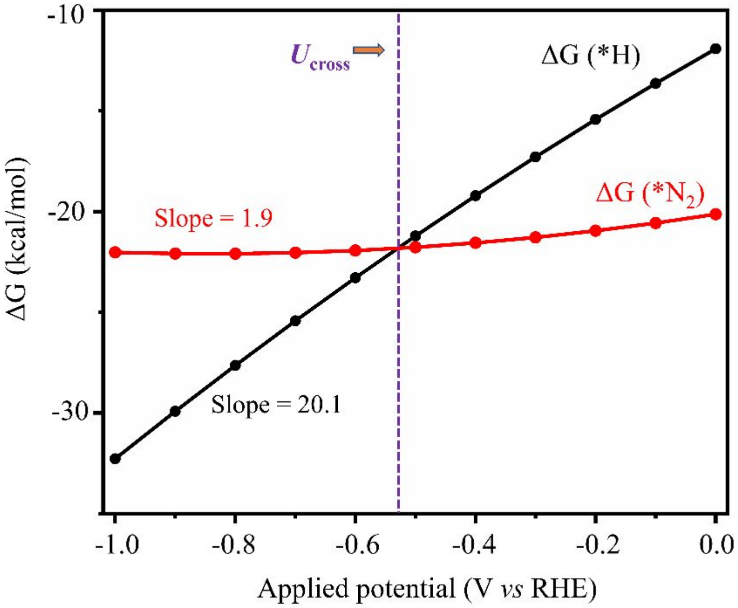

Figure 5: Free energy comparison between N_2 and H as a function of applied potential. To the left of U_{cross} = -0.51 hydrogen coverage starts to dominant the surface.

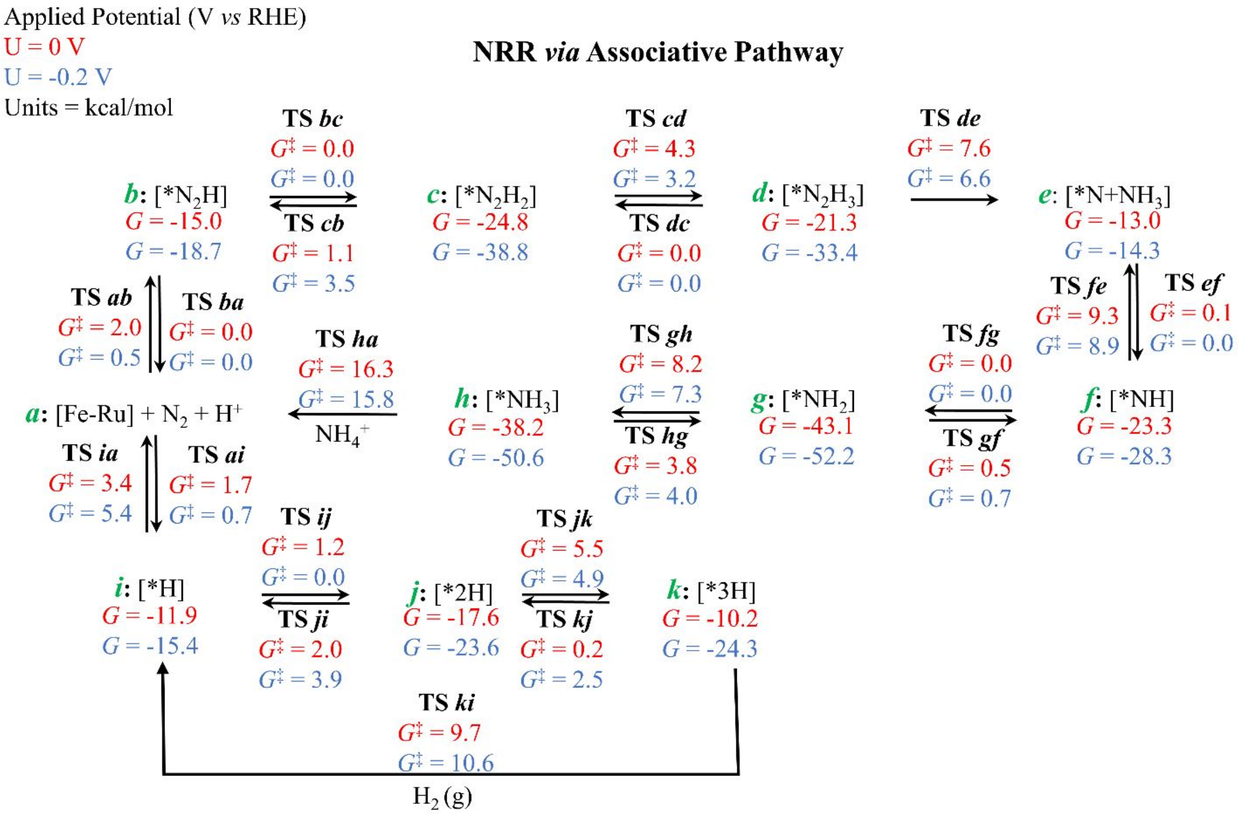

Figure 6: GCP profile along the reaction pathway for NRR and HER at two different potentials.

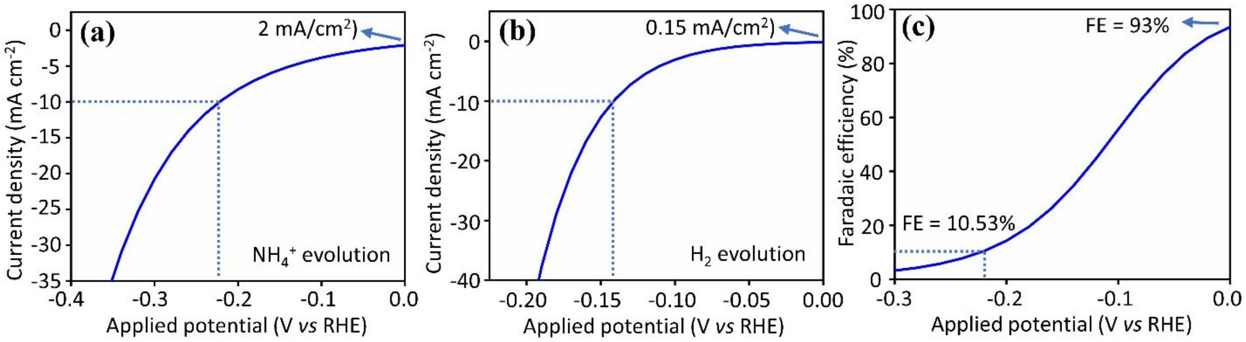

Figure 7: (a,b) QM predicted I-V curves for NRR and HER, (c) FE of ammonia as a function of applied potential. The 10 mA/cm^2 current for NH_3 is achieved at -0.22 V while for HER its -0.14 V. the FE is 10.53 % at -0.22 V.

Table 1: Species concentration

Species	Concentration at *U* = -0.2V, and 298.15K
x_a [Fe-Ru DAC]	2.9012E-10
X_b [$*N_2H$]	1.5995E-10
X_c [$*N_2H_2$]	5.6604E-08
X_d [$*N_2H_3$]	6.4478E-10
X_e [$*N + NH_3$]	2.197E-14
X_f [$*NH$]	5.7317E-12
X_g [$*NH_2$]	0.990763
X_h [$*NH_3$]	0.00474734
X_i [$*H$]	1.2403E-06
X_j [$*H_2$]	0.00437121
X_k [$*H_3$]	0.00011715